p38 Inhibition ameliorates skin and skull abnormalities in *Fgfr2* Beare-Stevenson mice

Yingli Wang,[1] Xueyan Zhou,[1] Kurun Oberoi,[1,2] Robert Phelps,[3,4] Ross Couwenhoven,[2,5] Miao Sun,[2,6] Amélie Rezza,[7,8] Greg Holmes,[1] Christopher J. Percival,[9] Jenna Friedenthal,[1] Pavel Krejci,[10,11] Joan T. Richtsmeier,[9,12] David L. Huso,[13] Michael Rendl,[4,7,8] and Ethylin Wang Jabs[1,2,8]

[1]Department of Genetics and Genomic Sciences, Mount Sinai School of Medicine, New York, New York, USA. [2]Department of Pediatrics, Institute of Genetic Medicine, Johns Hopkins University, Baltimore, Maryland, USA. [3]Department of Pathology and [4]Department of Dermatology, Mount Sinai School of Medicine, New York, New York, USA. [5]Department of Oncology and Diagnostic Sciences, University of Maryland Dental School, Baltimore, Maryland, USA. [6]Department of Medical Genetics and National Key Laboratory of Medical Molecular Biology, Institute of Basic Medical Sciences, Chinese Academy of Medical Sciences and Peking Union Medical College, Beijing, China. [7]Black Family Stem Cell Institute and [8]Department of Developmental and Regenerative Biology, Mount Sinai School of Medicine, New York, New York, USA. [9]Department of Anthropology, Pennsylvania State University, University Park, Pennsylvania, USA. [10]Medical Genetics Institute, Cedars-Sinai Medical Center, Los Angeles, California, USA. [11]Department of Animal Physiology and Immunology, Institute of Experimental Biology, Masaryk University and Department of Cytokinetics, Institute of Biophysics AS CR, Czech Republic. [12]Center for Functional Anatomy and Evolution and [13]Department of Molecular and Comparative Pathobiology, Johns Hopkins University School of Medicine, Baltimore, Maryland, USA.

Beare-Stevenson cutis gyrata syndrome (BSS) is a human genetic disorder characterized by skin and skull abnormalities. BSS is caused by mutations in the FGF receptor 2 (FGFR2), but the molecular mechanisms that induce skin and skull abnormalities are unclear. We developed a mouse model of BSS harboring a FGFR2 Y394C mutation and identified p38 MAPK as an important signaling pathway mediating these abnormalities. *Fgfr2^{+/Y394C}* mice exhibited epidermal hyperplasia and premature closure of cranial sutures (craniosynostosis) due to abnormal cell proliferation and differentiation. We found ligand-independent phosphorylation of FGFR2 and activation of p38 signaling in mutant skin and calvarial tissues. Treating *Fgfr2^{+/Y394C}* mice with a p38 kinase inhibitor attenuated skin abnormalities by reversing cell proliferation and differentiation to near normal levels. This study reveals the pleiotropic effects of the FGFR2 Y394C mutation evidenced by cutis gyrata, acanthosis nigricans, and craniosynostosis and provides a useful model for investigating the molecular mechanisms of skin and skull development. The demonstration of a pathogenic role for p38 activation may lead to the development of therapeutic strategies for BSS and related conditions, such as acanthosis nigricans or craniosynostosis.

Introduction

Beare-Stevenson cutis gyrata syndrome (BSS) (MIM #123709) is an autosomal dominant disorder characterized by both skin and skull abnormalities, including cutis gyrata, acanthosis nigricans (AN), craniosynostosis, craniofacial dysmorphism, including choanal atresia, a prominent umbilical stump, and anogenital anomalies (1–3). Patients can be born with respiratory distress and may die within 50 days after birth. Survivors have significant developmental delay (1, 4). Skin abnormalities such as cutis gyrata and AN are common characteristics of this genetic disease (3). Cutis gyrata is characterized by furrowed skin with a corrugated appearance. The skin may exhibit hyperplasia of connective tissue histologically (3). AN presents as a brown-to-black, poorly defined, velvety hyperpigmentation of the skin, with a prevalence of 7% in unselected populations (5–7). Histologic evaluation of AN is characterized by hyperkeratosis and papillomatosis, with a thinned epidermis overlying the papillae. Acanthosis is usually confined to the troughs of the epidermal papillae, and hyperpigmentation is not always present (8, 9). Craniosynostosis, a common isolated congenital disorder, is characterized by premature fusion of sutures and abnormal cranial vault shape. It can also be associated with midfacial hypoplasia as well as increased intracranial pressure. Craniosynostosis occurs in 1 in 2,500 newborns across all ethnicities and is

present in more than 100 human skeletal syndromes (10–13). The FGF receptor (FGFR) mutations that underlie the genetic basis of BSS are FGFR2 Y375C and S372C (human FGFR2 IIIc protein NP_000132.3) of the juxtamembrane domain (4, 14–19).

The FGF/FGFR family is involved in the regulation of normal development of the skin and cranial vault (20–23). The skin is derived from the embryonic ectoderm and consists of the epidermis and dermis. The epidermis is a stratified epithelium that contains a proliferating basal layer and multiple differentiating layers, including the spinous, granular, and cornified layers. It is maintained by self-renewable epithelial stem cells in the basal layer that produce progenies that undergo terminal differentiation into various types of cells (21, 24). Calvarial sutures are the unossified regions of mesenchymal cells that form between the opposing osteogenic fronts of intramembranous bones of the cranial vault (25).

Studies of gene expression and transgenic mice have revealed important roles for FGFs and FGFRs, not only in keratinocytes during skin development and homeostasis (26–31), but also in osteoblasts during calvarial development (32–35). FGFR2 IIIb is localized predominantly in the basal and suprabasal keratinocyte layer (27–32, 36). FGFR2 IIIb transgenic mice expressing a dominant-negative receptor in keratinocytes under a K14 promoter or mice deficient for Fgfr2 IIIb in all cells showed epidermal atrophy and hair follicle abnormalities (26–28). Mice lacking the IIIb splice variants of Fgfr1 and Fgfr2 in keratinocytes under a K5 promoter showed a slight epidermal hypotrophy in very young mice, and with age, the mice
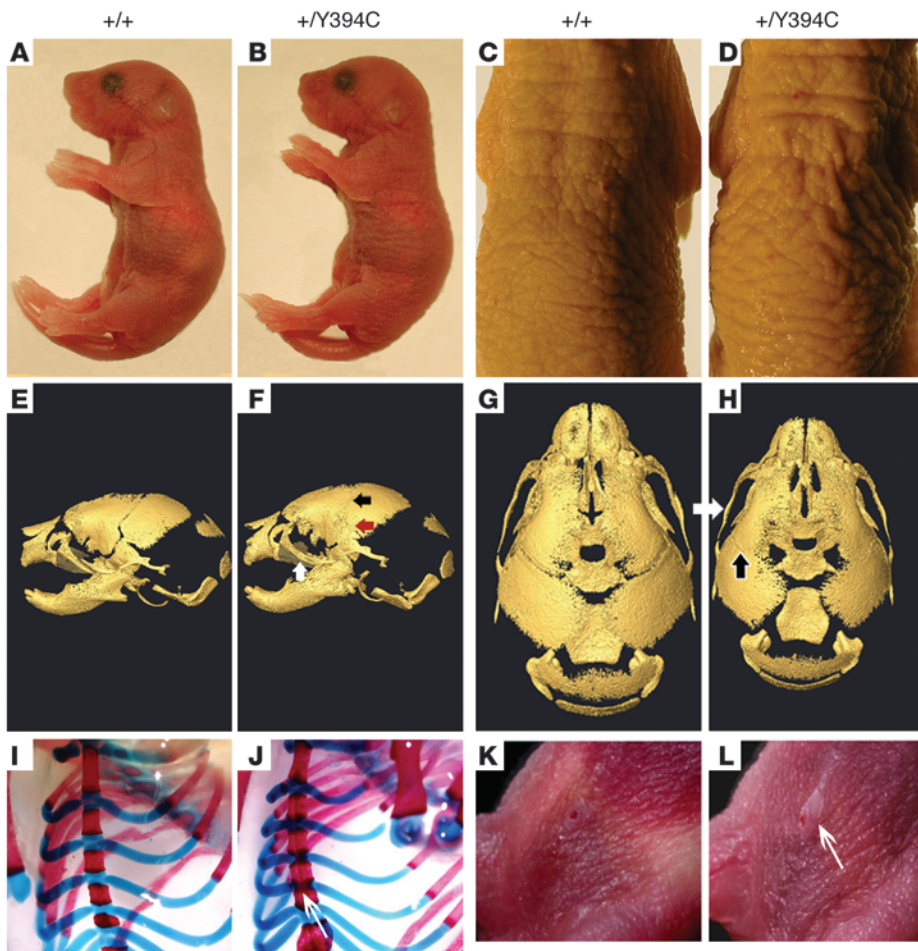
Figure 1
Fgfr2+/Y394C mice have cutis gyrata, acanthosis, skull synostosis, and other abnormalities. (**A**–**D**) Note skin furrows and hyperplasia in the mutant mice at P0 (**A** and **B**). With age, the skin phenotype becomes more obvious at P3 (**C** and **D**). (**E**–**H**) Surface reconstructions of HRCT images show midfacial hypoplasia of the mutant mice at P0. Note premature fusion of the coronal suture (**E**–**H**; black arrows), zygomaxillary suture (**E**–**H**; white arrows), and squamosal suture (**E**–**H**; red arrow) (Supplemental Table 1). (**I** and **J**) Alizarin red S and Alcian blue staining of the chest show abnormal bony fusion of sternum in mutant at P0. (**K** and **L**) Gross observations reveal protruding and enlarged umbilical stump in mutant (arrow). **A**, **C**, **E**, **G**, **I**, and **K** are from littermate controls. **B**, **D**, **F**, **H**, **J**, and **L** show the corresponding organs and tissues in mutant mice.

manifested keratinocyte hyperproliferation with the onset of inflammation (30, 31). FGFR2 IIIc is expressed in preosteoblasts and osteoblasts in both endochondral and intramembranous ossification (37). These studies suggest that FGFR2 plays an important role in the regulation of both epidermal maintenance and bone development.

FGFs bind to the linker region between the extracellular immunoglobulin-like domains, IgII and IgIII, of FGFR2. When the receptor is dimerized and phosphorylated, it activates downstream signaling pathways to control the balance among different cellular activities, including migration, proliferation, differentiation, and survival of cells (32, 38–40). The 2 main FGFR2 isoforms, epithelial FGFR2 IIIb and mesenchymal FGFR2 IIIc, show distinct ligand specificity for different FGF ligands (41–43). To date, no functional studies on the BSS mutant FGFR2 have been performed. FGFR2 is known to signal by several downstream pathways including the MAPKs ERK1/2 and p38, PI3K/AKT, PLCγ pathways, and others, depending on cell type, tissue-specific expression, and developmental processes (22, 39, 44, 45). The MAPK pathways are critical in normal epidermal development (46). Although studies have suggested that alteration of FGFR2 and its downstream pathways contribute to craniosynostosis conditions (22, 33, 47–51), the mechanism by which cranial vault and skin abnormalities, especially cutis gyrata and acanthosis, are induced remains unclear.

To understand the cellular and molecular pathogenesis of the skin and skull malformations in BSS and to provide information relevant to possible molecular approaches for treatment of the skin and skull abnormalities, we created the first mouse model for BSS with cutis gyrata and acanthosis by introducing the FGFR2 Y394C mutation (mouse FGFR2 IIIc protein NP_034337.2, analogous to the Y375C substitution in humans) into the mouse genome using a knockin approach. Our analysis showed that mutant mice exhibit epidermal hyperplasia and craniosynostosis of the calvarial sutures, which are accompanied by abnormal proliferation and differentiation of keratinocytes and osteoblasts, respectively. We found constitutive activation of the FGFR2 receptor and the activation of MAPK p38 signaling in the mutant epidermis and skull. Our data demonstrate that pharmacological blockade of p38 activation partially suppressed epidermal hyperplasia and, to a lesser degree, premature closure of the coronal suture in *Fgfr2+/Y394C* mice, correlating with attenuated hyperproliferation and normal expression of differentiation markers. Our findings provide opportunities for dissecting the molecular mechanisms of BSS and developing novel therapeutic strategies related to similar, more common conditions of acanthosis nigricans or craniosynostosis.

Results

Fgfr2+/Y394C mice show epidermal abnormalities similar to those in human BSS. We created a mouse model for BSS by designing a gene-targeting construct to site-specifically knock in the mutation *Fgfr2* 1181A>G by homologous recombination (Supplemental Figure 1, A and B; supplemental material available online with this article; doi:10.1172/JCI62644DS1). In heterozygous *Fgfr2+/Y394C* mice, the
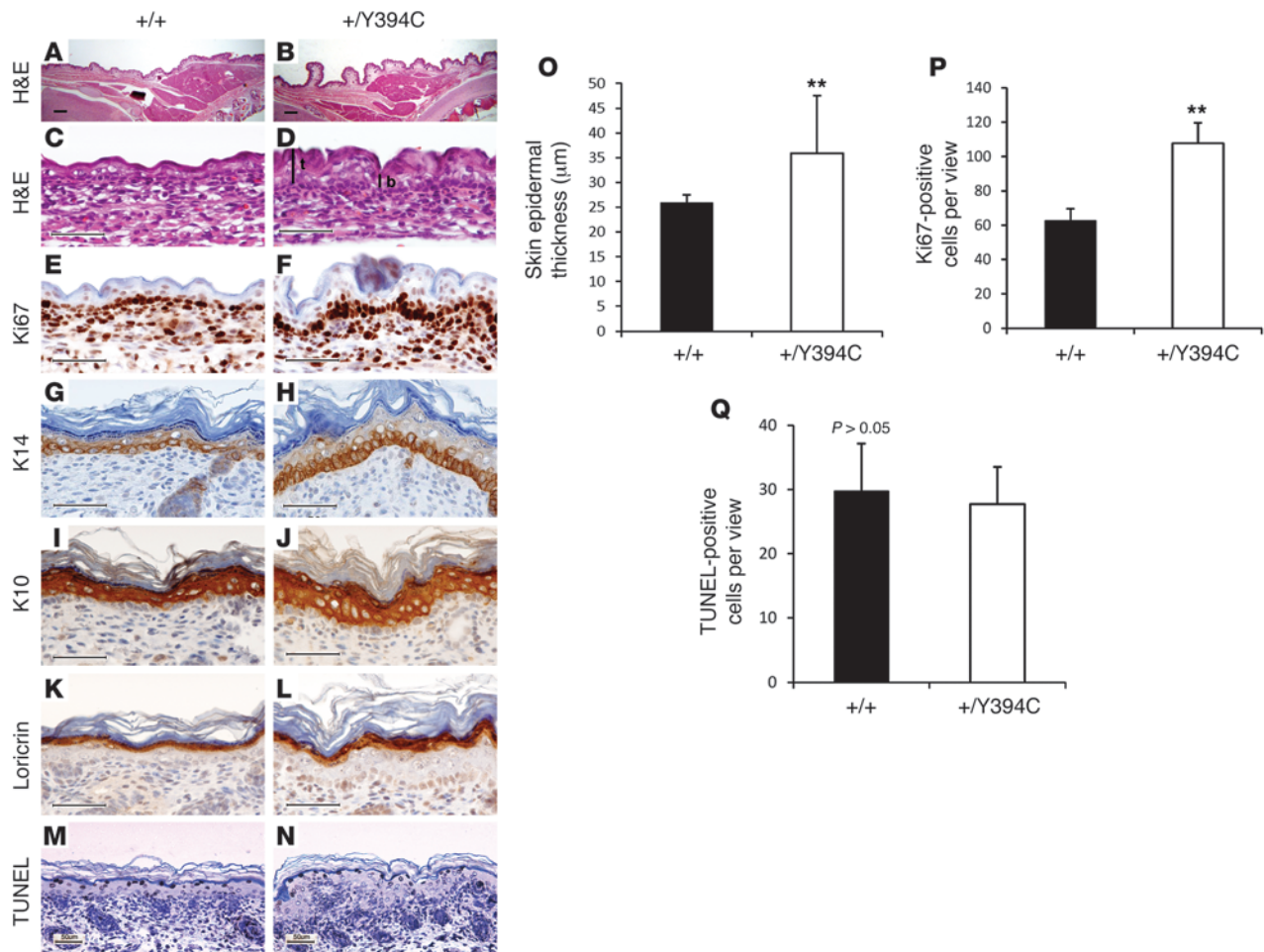
Figure 2
Fgfr2+/Y394C mice show abnormal histology, proliferation, and differentiation in the epidermis. (**A–D**) H&E staining shows the abnormal development of the mutant skin with cutis gyrata (corrugation), epidermal hyperplasia, and thickening at E16.5 and P0. The measurements of the thickness were performed at the top (t) and the bottom (b) of the troughs of the papillomatosis in the mutants. (**E** and **F**) Immunohistochemical staining of Ki67 shows increased numbers of positive cells in the basal layer of mutant epidermis at E16.5. (**G–L**) Immunohistochemical staining of differentiation markers show abnormal differentiation of (**G** and **H**) expression of K14 for basal layer, (**I** and **J**) expression of K10 for spinous layer, and (**K** and **L**) expression of loricrin for cornified and granular layers. (**M** and **N**) TUNEL mutant epidermis staining shows slight decrease of apoptosis in mutants. (**O–Q**) Bar graphs show epidermal thickening (**O**), increased number of Ki67-positive cells (**P**), and no obvious change in apoptosis in mutants (**Q**). A, C, E, G, I, K, and M are from littermate controls. B, D, F, H, J, L, and N show the corresponding organs and tissues in mutant mice. Scale bars: 200 μm (**A** and **B**); 50 μm (**C–N**). Results are presented as mean ± SEM. **$P < 0.01$.

mutant *Fgfr2* allele generates a number of transcripts similar to that of the WT allele in both skull and skin tissues (Supplemental Figure 1B). At early postnatal stage P0, the *Fgfr2+/Y394C* mice could be distinguished macroscopically from their littermate controls by skin furrowing and dome-shaped heads (Supplemental Figure 1C), and with age the mutants showed reduced growth and early death, usually within 2 weeks (Supplemental Figure 1, D–F). Necropsy of P0 *Fgfr2+/Y394C* mice revealed multiple malformations in the skin, skull, sternum, and umbilicus, which resemble those of the human condition (refs. 1–3 and Figure 1). Each of these different defects showed 100% penetrance in mutant mouse. The mutant skin displayed typical furrowing and thickening, similar to the cutis gyrata and acanthosis observed in BSS patients (Figure 1, A–D). High-resolution micro-CT scans of *Fgfr2+/Y394C* mice revealed midfacial hypoplasia, brachycephalic-shaped skull, and premature fusion of coronal and other sutures (Figure 1, E–H, and Supplemental Figure 2). Morpho-

metric analysis of 3D craniofacial landmarks showed comparable statistically significant differences between *Fgfr2+/Y394C* and controls at P0 and at P8, with the dysmorphology becoming more pronounced by P8 (Supplemental Table 1 and Supplemental Figure 2). Other abnormalities included fusion of bones of the sternum (Figure 1, I and J) and an enlarged umbilical stump (Figure 1, K and L).

Detailed characterization of skin and skull abnormalities was performed, as these 2 phenotypes are the major features in BSS patients (3). Histologically, the skin of E16.5, P0, and P5 *Fgfr2+/Y394C* mice displayed cutis gyrata, epidermal acanthosis, and papillomatosis (Figure 2, A–D). The thickness of the epidermis was significantly different between the mutant and WT (+/Y394C [$n = 12$] versus +/+ [$n = 12$] at E16.5: 35.9 ± 11.6 μm versus 25.9 ± 1.6 μm, $P < 0.006$; +/Y394C [$n = 12$] versus +/+ [$n = 12$] at P0: 48.8 ± 13.9 μm versus 27.1 ± 3.3 μm, $P < 0.000007$; +/Y394C [$n = 6$] versus +/+ [$n = 6$] at P5: 44.6 ± 4.3 μm versus 26.7 ± 2.6 μm, $P < 0.000005$) (Figure 2, C,
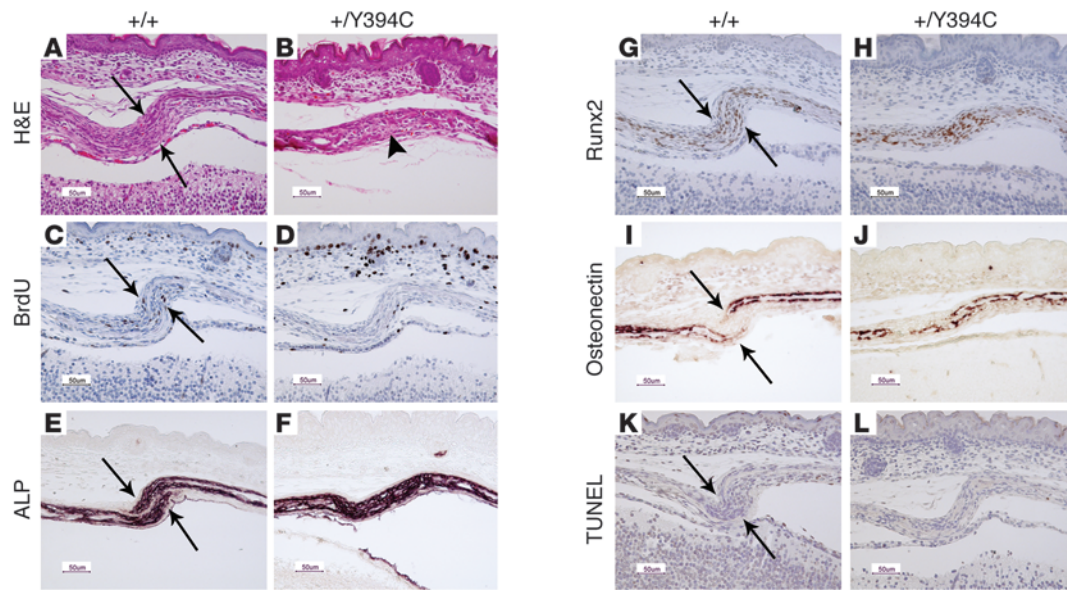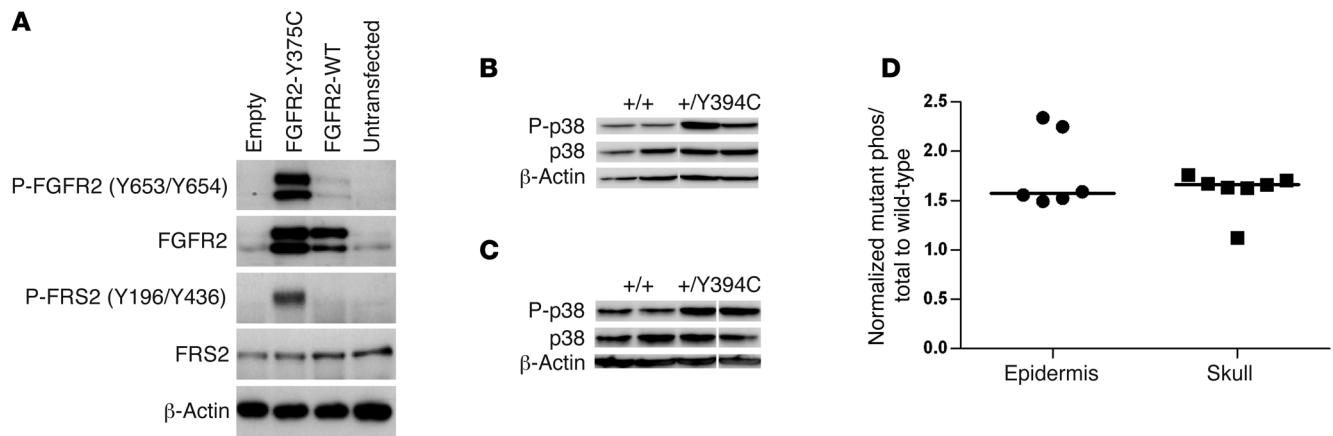
Figure 3
Fgfr2+/Y394C mice show abnormal histology, proliferation, and differentiation in the skull. (**A** and **B**) H&E staining shows the abnormal development of the mutant coronal suture at E17.5, with presynostosis and osteoid deposition between the osteogenic fronts (arrows, osteogenic fronts; arrowhead, presynostosis/synostosis). (**C** and **D**) Immunohistochemical staining of BrdU shows decreased numbers and abnormal distribution of positive cells in mutants at E17.5. (**E** and **F**) ALP staining shows broad and expanded ALP expression into the coronal suture of the mutants at E17.5. (**G** and **H**) Immunohistochemical staining of Runx2 shows increased expression and abnormal differentiation at the osteogenic fronts at E17.5. (**I** and **J**) In situ hybridization of osteonectin shows accelerated bone formation in mutants at E17.5. (**K** and **L**) TUNEL staining shows no obvious change of apoptosis in the mutant. **A**, **C**, **E**, **G**, **I**, and **K** are from littermate controls. **B**, **D**, **F**, **H**, **J**, and **L** show the corresponding organs and tissues in mutant mice. Scale bars: 50 μm.

D, and O, and Figure 3, A and B). The height measurements of the top and bottom of the troughs of the papillomatosis showed significant differences in mutants from E16.5 to P0 (E16.5: top, mean 46.8 ± 4.5 μm versus bottom, mean 25.1 ± 2.5 μm; P0: 59.8 ± 9.3 μm to 37.7 ± 7.0 μm); thus the averages of the overall heights were significantly different and displayed greater statistical variation as compared with those of the controls (+/Y394C [n = 12] versus +/+ [n = 12] at E16.5: 35.9 ± 11.6 μm versus 25.6 ± 1.6 μm, $P < 9 \times 10^{-13}$; +/Y394C [n = 12] versus +/+ [n = 12] at P0, 48.8 ± 13.9 μm to 27.1 ± 3.3 μm, $P < 1.3 \times 10^{-6}$) (Figure 2O, E16.5). The thickness of the dermis was not significantly different between mutant and WT (+/Y394C [n = 12] versus +/+ [n = 12] at P0: 146.7 ± 14.2 μm versus 140.8 ± 39.2 μm, P > 0.05; +/Y394C [n = 6] versus +/+ [n = 6] at P5: 533.3 ± 51.6 μm versus 487.5 ± 23.6 μm, P > 0.07). WT and mutant epidermis were stained with Masson-Fontana from P0 to P7, and only patchy melanin and dendritic melanocytes were present in the stratum basale. Most of the melanin and melanocytes were in the matrix of the hair follicles. No clear difference could be discerned between the 2 groups (Supplemental Figure 3, A and B).

The basal layer of the epidermis was particularly affected by proliferative changes as compared with that of the WT littermates. Quantitation of cell proliferation in the epidermis showed that *Fgfr2+/Y394C* mice showed a 2-fold increase in Ki67-positive cell numbers compared with controls (E16.5: +/Y394C [n = 4] versus +/+ [n = 4]: 107.7 ± 12.0 versus 62.8 ± 6.7, P < 0.01; P0: +/Y394C [n = 4] versus +/+ [n = 4]: 38.2 ± 5.7 versus 19.8 ± 3.5, P < 0.01) (Figure 2, E, F, and P, E16.5). The cell proliferation in the dermis was the same in the mutant and WT (+/Y394C [n = 6] versus +/+ [n = 6] at P0: 94 ± 13.9 versus 83 ± 5.2, P > 0.09).

Immunohistochemical analysis of epidermal differentiation markers revealed increased expression due to hyperplastic cells in each layer, including keratin 14 (K14) in the basal layer (Figure 2, G and H), K10 in the spinous layer (Figure 2, I and J), and loricrin in the granular as well as cornified layers (Figure 2, K and L) in mutant mice, but none of these markers was ectopically expressed beyond the layer of regular detection. There were slightly, but not significantly, fewer apoptotic cells in the epidermis of *Fgfr2+/Y394C* mice relative to controls as determined by quantitation of TUNEL staining (+/Y394C [n = 2] versus +/+ [n = 3]: 29.8 ± 7.4 versus 27.7 ± 5.8, P > 0.05) (Figure 2, M, N, and Q). We also examined the development of hair follicles and did not find obvious differences in developmental timing, numbers, distribution, or structure between mutants and controls (Supplemental Figure 3). Permeability assays suggested a normal epidermal barrier in mutant mice as compared with controls from E14.5 to E18.5 (data not shown).

Fgfr2+/Y394C mice have skull synostosis with abnormal proliferation and differentiation. The coronal suture of the skull was examined microscopically at different developmental stages. In *Fgfr2+/Y394C* mice at E17.5, the coronal sutures exhibited synostosis and presynostosis, a condition characterized by proximate osteogenic fronts, showing deposition of osteoid as compared with the clearly separated fronts in controls (Figure 3, A and B). Cell proliferation was analyzed by calculating the ratios of the number of BrdU-positive cells to total cells between and including the osteogenic fronts in mutants and littermate controls. At E17.5, the ratio was obviously decreased in mutants as compared with controls (+/Y394C [n = 3] versus +/+ [n = 3]: 0.05 ± 0.02 versus 0.13 ± 0.02, P = 0.004) (Figure 3, C and D). Differentiation of the coronal suture was studied

Figure 4
Constitutive activation of human FGFR2 Y375C in culture and increased phosphorylation of p38 in the epidermis and skull of *Fgfr2*[+/Y394C] mice. (**A**) Immunoprecipitation and Western blot analysis show constitutive activation of FGFR2 receptor and FRS2 in RCS chondrocytes transfected with human FGFR2 Y375C as compared with WT controls. (**B** and **C**) Western blot analysis shows increased phosphorylated p38 in epidermis (**B**) and skull tissues (**C**) Lanes were run on the same gel, but were noncontiguous. (**D**) Scatter plots using normalized levels of mutant[phos/total]/control[phos/total] show an increased ratio of phosphorylated p38 to total protein in the epidermis and skull tissues of *Fgfr2*[+/Y394C] mice as compared with the WT controls. Each dot represents the analysis of data from 1 embryo. Bar represents median value.

from E17.5 to P0 by using alkaline phosphatase (ALP), Runx2, osteopontin, and osteonectin markers. Apparent differences in the expression of these markers were found between mutants and controls. In mutants, the coronal suture exhibited ALP expression in the region between the 2 osteogenic fronts, whereas there was no ALP expression in the same region of controls (Figure 3, E and F). The staining of Runx2 also showed increased expression in the area between the 2 osteogenic fronts in mutants as compared with controls (Figure 3, G and H). Expression of osteonectin showed more overlap of the osteogenic fronts (Figure 3, I and J). These data indicated increased osteogenic differentiation as well as abnormal bone growth at the coronal suture in *Fgfr2*[+/Y394] mice. There was no obvious difference in apoptosis between mutants and controls at E17.5 and P0 (Figure 3, K and L). These results showed that the epidermal hyperplasia as well as premature fusion of the coronal sutures of *Fgfr2*[+/Y394C] mice are associated with aberrant proliferation and differentiation.

The Y394C mutation causes constitutive activation of FGFR2 in rat chondrosarcoma chondrocytes and keratinocytes of Fgfr2[+/Y394C] *mice.* To learn about the mechanisms underlying the FGFR2 Y394C mutation in BSS, we analyzed the effect of this mutation on the receptor function. Our results showed constitutive activation of FGFR2 receptor and FRS2, a major FGFR downstream mediator (52), in rat chondrosarcoma (RCS) chondrocytes transfected with human FGFR2 Y375C as compared with WT FGFR2 (Figure 4A). We confirmed this result in vivo by demonstrating increased phosphorylation of FGFR2 in epidermal keratinocytes derived from our *Fgfr2*[+/Y394C] mice without the addition of FGF ligand as compared with that of controls (Supplemental Figure 4), indicating that the Y394C mutation causes constitutive or ligand-independent activation of the receptor.

The Y394C mutation causes activation of MAPK p38 kinase. We further investigated the signaling pathways downstream of FGFR2, including ERK1/2, p38, JNK, and PI3K/AKT pathways in epidermis and skull tissues of *Fgfr2*[+/Y394C] mice. The median phosphorylated p38 levels were increased about 1.5-fold in both

tissues as compared with controls (Figure 4, B–D). None of the other pathways showed obvious changes of phosphorylation in both tissues; however, we noted phosphorylated ERK1/2 was increased in mutant skull tissues (Supplemental Figure 5). These results indicate that the FGFR2 Y394C mutation contributes to the constitutive activation of the receptor and the activation of the downstream pathway p38 MAPK in both the epidermis and skull.

In utero systemic p38 inhibition attenuates epidermal and skull abnormalities as well as abnormal proliferation and differentiation in Fgfr2[+/Y394C] *mice.* To further study the relationship between p38 signaling and the skin and skull abnormalities in the mutant mice, we inhibited p38 activity by intraperitoneally injecting either SB203580, a p38 kinase inhibitor (53), or a PBS-vehicle control into pregnant females from E12.5 to E18.5. We used SB203580 because it is a pyridinyl imidazole inhibitor that specifically inhibits p38 kinase activity in an ATP-competitive manner. It has been extensively investigated in targeting p38 signaling in preclinical mouse models with different conditions, including inflammatory disease, cancer, pulmonary disease, and bone disorders (53, 54). We examined the phosphorylation of p38 in the epidermis of offspring after drug administration at P0. The PBS-treated mutant epidermis had high levels of phosphorylated p38, which was dramatically reduced in mutants treated with SB203580, indicating that this drug inhibited p38 activity successfully in vivo (Figure 5, A and B). Macroscopically, the skin showed slight improvement in the SB203580-treated mutant mice compared with the PBS-treated and untreated mutants. Histological examination of PBS-treated *Fgfr2*[+/Y394C] mice revealed typical skin phenotypes with epidermal hyperplasia and thickening at P0 (+/Y394C [*n* = 3] versus +/+ [*n* = 3]: 43.9 ± 1.7 μm versus 31.0 ± 0.7 μm, *P* < 0.01), whereas mutant mice treated with SB203580, showed that 59% of the microscopic views of the epidermis (31 out of 52 serial histological views of 9 mutant pups from 3 different litters) were histologically normal and the hyperplasia-driven thickening was decreased as compared with those of the PBS-treated mice (+/Y394C [*n* = 3] versus +/+ [*n* = 3]: 28.3 ± 2.4 μm versus 26.8 ± 5.0 μm, *P* > 0.05) (Figure 5, C–F, and W).
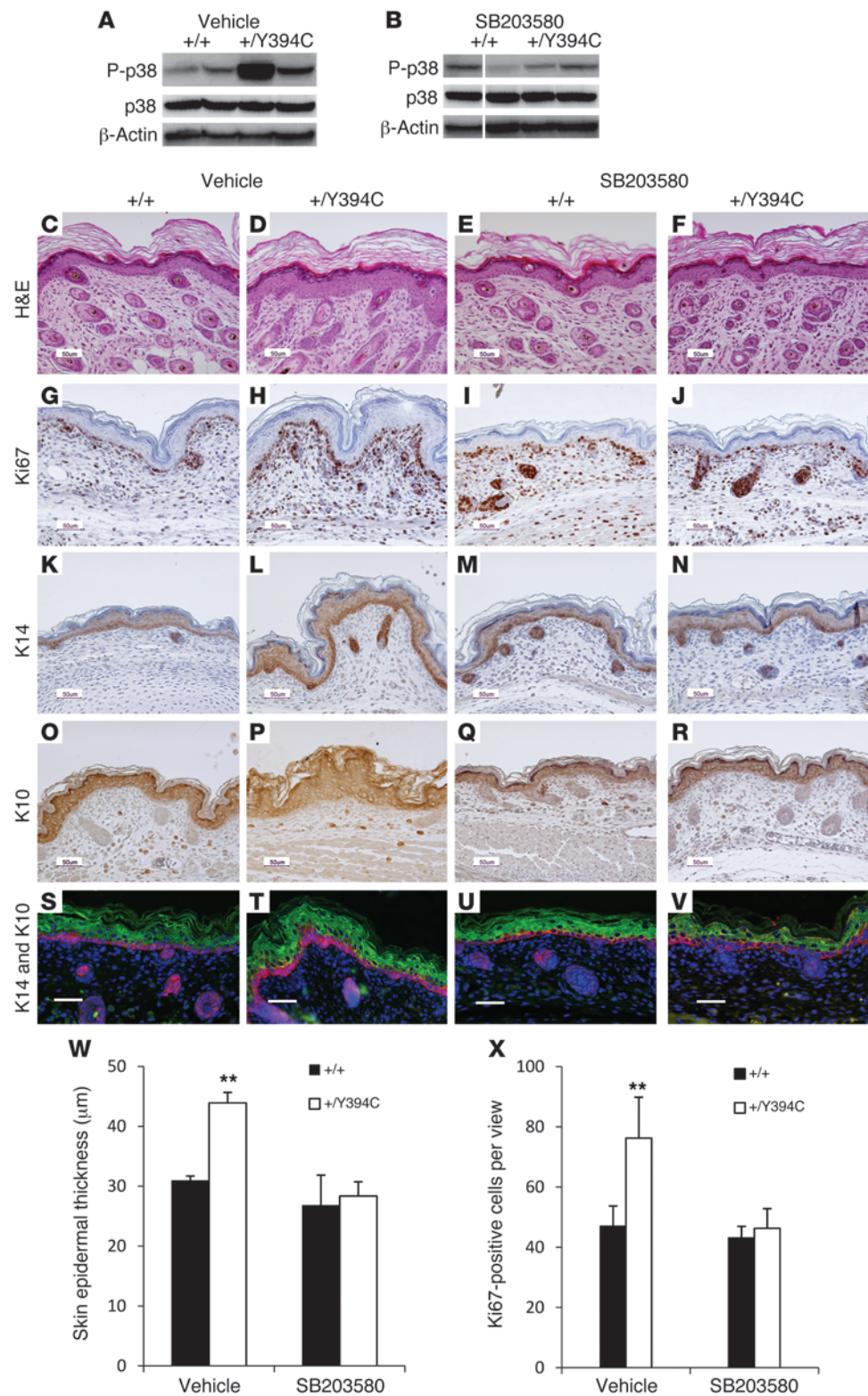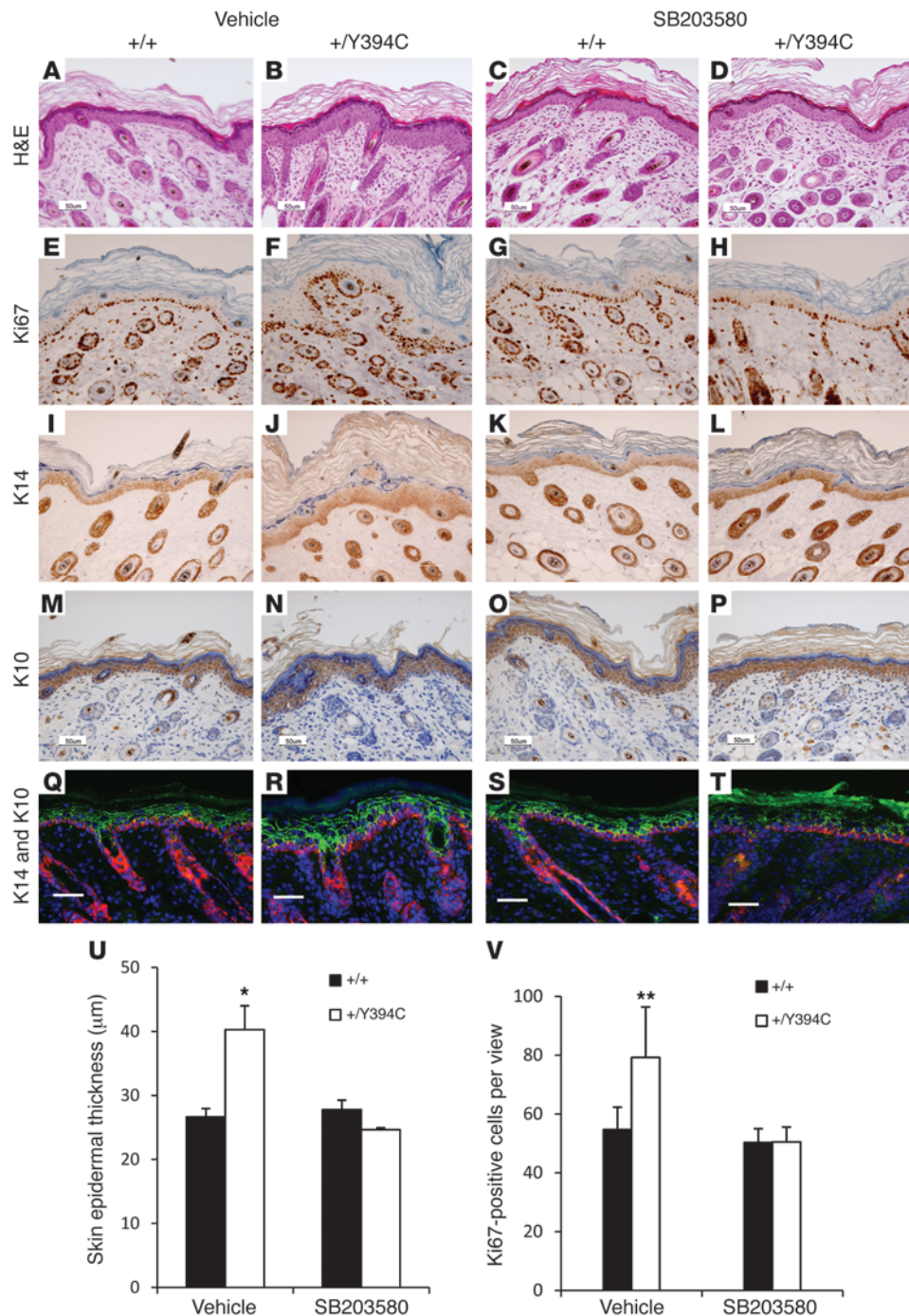
Figure 5
In utero systemic p38 inhibition attenuates skin abnormalities in *Fgfr2+/Y394C* mice. (**A** and **B**) Western blot analysis shows increased phosphorylated p38 level in *Fgfr2+/Y394C* epidermis treated with PBS (**A**) and relatively normal phosphorylated p38 level in *Fgfr2+/Y394C* epidermis treated with SB203580 compared with the controls (**B**). Lanes were run on the same gel, but were noncontiguous. (**C**–**F**) H&E staining shows epidermal hyperplasia in *Fgfr2+/Y394C* mice treated with PBS (**C** and **D**), and SB203580 treatment rescued skin phenotype in mutants (**E** and **F**). (**G**–**J**) Ki67 staining shows increased number of Ki67-positive cells in the basal layer of PBS-treated mutants (**G** and **H**); hyperproliferation in the mutant epidermis was reduced after SB203580 treatment (**I** and **J**). (**K**–**V**) Staining of differentiation markers of epidermis shows increased expression of the markers in the basal (K14, **K**, **L**, **S**, and **T**) and spinous layers (K10, **O**, **P**, **S**, and **T**) of PBS-treated mutant mice; SB203580 treatment reduced the expression of these markers (K14, **M**, **N**, **U**, and **V**; K10, **Q**, **R**, **U**, and **V**). Scale bars: 50 μm. (**W** and **X**) Bar graph shows that the epidermal thickening (**W**) and the number of Ki67-positive cells (**X**) of mutants after the SB203580 treatment compared with those of the vehicle-treated mice. Results are presented as mean ± SEM. **$P < 0.01$.

We further analyzed the skin of PBS- or SB203580-treated pups for Ki67 staining and expression of differentiation markers. Upon PBS treatment, *Fgfr2+/Y394C* mice displayed 1.9 times as many proliferating cells in the basal layer as littermate controls (+/Y394C [$n = 4$] versus +/+ [$n = 4$]: 76.3 ± 13.6 versus 47.0 ± 6.7, $P < 0.05$) (Figure 5, G, H, and X) as well as increased expression of K14 in the basal layer (Figure 5, K, L, S, and T) and K10 in the spinous layer (Figure 5, O, P, S, and T), similar to the results without treatment. In contrast, upon SB203580 treatment, *Fgfr2+/Y394C* mutant skin displayed only 1.1 times as many proliferating cells in the basal layer compared

Figure 6
Topical p38 inhibition attenuates skin abnormalities in *Fgfr2+/Y394C* mice. The skin on the back of *Fgfr2+/Y394C* mice and littermate controls was treated with SB203580 or vehicle control. (**A–D**) H&E staining shows typical epidermal hyperplasia in *Fgfr2+/Y394C* mice treated with vehicle (**A** and **B**); SB203580 treatment rescued the skin phenotype in mutant mice (**C** and **D**). (**E–H**) Immunohistochemical staining of Ki67 shows increased number of Ki67-positive cells in the basal layer of vehicle-treated mutant mice (**E** and **F**); the hyperproliferation in the mutant epidermis was reduced after SB203580 treatment (**G** and **H**). (**I–T**) Immunohistochemical staining of differentiation markers of epidermis shows increased expression of the markers in the basal (K14, **I**, **J**, **Q**, and **R**) and spinous layers (K10, **M**, **N**, **Q**, and **R**) of vehicle-treated mutant mice; SB203580 treatment reduced the expression of these markers (K14, **K**, **L**, **S**, and **T**; K10, **O**, **P**, **S**, and **T**). Scale bars: 50 μm. (**U** and **V**) Bar graphs show that the epidermal thickening (**U**) and the increased number of Ki67-positive cells (**V**) of mutants were reversed after the SB203580 treatment. Results are presented as mean ± SEM. *$P < 0.05$; **$P < 0.01$.

with WT controls (+/Y394C [$n = 4$] versus +/+ [$n = 4$]: 46.3 ± 6.5 versus 43.1 ± 3.8, $P > 0.05$) (Figure 5, I, J, and X). The expression of K14 and K10 also decreased to a level and distribution similar to that of the WT controls (Figure 5, M, N, U, and V [K14]; Figure 5, Q, R, U, and V [K10]).

Initial qualitative examination of the specimens showed that about half of the *Fgfr2+/Y394C* mice (5 in 9 pups from 3 litters) treated with SB203580 had a relatively normal head shape at P0 (Supplemental Figure 6, A–C), but subsequent landmark-based quantification of skull morphology did not show significant differences between treated and untreated mutants (data not shown). The histological evaluation at comparable levels of the skull did not reveal obvious improvement in most of the mutant mice with drug treatment, as compared with the fused sutures of untreated or PBS-treated mutants. Only a small portion of drug-treated mutant pups (20% of mutants from 2 litters) showed slight improvement and increased patency in coronal sutures. These findings were further confirmed by ALP staining (Supplemental Figure 6, D–I). We also examined the phosphorylation of p38 in the skull of pups after drug administration at P0 by immunohistochemical staining. Our results showed that the treatment of SB203580 reduced the level of phosphorylated p38

in coronal sutures of mutants compared with those untreated mutants, indicating that the drug inhibited p38 activity successfully in the skull (Supplemental Figure 6, J–L). Although systemic administration showed varying results, these data indicated that this SB203580 dosage treatment did ameliorate skin abnormalities and had certain cellular, but not appreciable, morphologic effect on skull abnormalities in the $Fgfr2^{+/Y394C}$ mice.

Previous studies have shown that ERK1/2 and p38 are important pathways that may mediate the premature closure of sutures in Apert syndrome $Fgfr2^{+/S252W}$ and $Fgfr2^{+/P253R}$ mice (47, 49, 50). We treated our BSS $Fgfr2^{+/Y394C}$ mice with MEK/ERK inhibitor U0126 at previously published dosages (47), but the inhibition did not reveal obvious rescue of the skin and skull phenotypes (data not shown). We also treated Apert $Fgfr2^{S252W/+}$ mice on the same C57BL/6J background and same dosage of SB203580 as our BSS mice to target the p38 kinase with no obvious improvement in skull morphology (data not shown). These results also suggested that p38 modulation is more effective for treatment of skin phenotypes and to a lesser degree for cranial vault phenotypes in these craniosynostosis mouse models. The SB203580 treatment did not improve the survival rate of $Fgfr2^{+/Y394C}$ mice, suggesting that other or multiple malformations cause the neonatal lethality and that refined or alternative treatment strategies are required.

Topical p38 inhibition attenuates skin abnormalities as well as abnormal epidermal proliferation and differentiation of $Fgfr2^{+/Y394C}$ mice. To use a more direct approach and avoid undue systemic effects, we used topical treatment to downregulate p38 kinase specifically in the skin. The administration of SB203580 obviously repressed the epidermal hyperplasia and thickening in the mutants (+/Y394C [$n = 3$] versus +/+ [$n = 3$]: 24.6 ± 0.3 μm versus 27.8 ± 1.5 μm, $P > 0.05$) compared with those of the vehicle-treated mice (+/Y394C [$n = 3$] versus +/+ [$n = 3$]: 40.3 ± 3.7 μm versus 26.6 ± 1.3 μm, $P < 0.01$) (Figure 6, A–D, and U). In drug-treated $Fgfr2^{+/Y394C}$ mice, the number of Ki67-positive cells (+/Y394C [$n = 4$] versus +/+ [$n = 4$]: 50.5 ± 5.0 versus 50.3 ± 4.7, $P > 0.05$) (Figure 6, E–H, and V) and expression of K14 and K10 (Figure 6, I–T) were similar to those of WT littermate controls, as opposed to those in vehicle-treated control mice (+/Y394C [$n = 4$] versus +/+ [$n = 4$]: 79.2 ± 17.2 versus 54.7 ± 7.6, $P < 0.01$). Thus, p38 signaling exerts an important influence in skin development in $Fgfr2^{+/Y394C}$ mice.

Discussion

Mice carrying the heterozygous Y394C mutation of the *FGFR2* gene serve as an important mouse model showing both skin and skeletal defects. In our in vivo mouse model, we observed consistent skin furrowing/corrugation and hyperplasia as well as synostosis of the coronal sutures. High penetrance of affected organs in this mouse model indicates that FGFR2 and its downstream pathways are crucial to the pleiotropic effects on skin and skull. The skin lesions observed in our $Fgfr2^{+/Y394C}$ mouse model are consistent with human cutis gyrata and AN. The epidermis showed epidermal acanthosis and papillomatosis, as has been described for the human counterpart. The absence of increased pigment is not surprising, as that is not always present with AN, and other mice reported with acanthosis in the context of diseases such as benign tumors or psoriasis also do not have hyperpigmentation (55, 56), possibly due to strain or species differences. In the different layers of the epidermis, the $Fgfr2^{+/Y394C}$ mutant mice had an increased number of proliferating cells in the basal layer and abnormal differentiation. Our studies and the work of others have provided evidence that FGFR signaling

is also involved in the proliferation and differentiation of calvarial osteoblasts from patients and sutural development in $Fgfr2^{+/Y394C}$ and other craniosynostosis mouse models (22, 33, 35, 48, 49). Collectively, these findings demonstrate that FGFR2 signaling regulates the disturbances of proliferation and differentiation in both the developing skin and skeleton.

Besides BSS, cutaneous phenotypes have been found in other congenital skeletal disorders caused by FGFR mutations. For example, there is AN in Crouzonodermoskeletal syndrome caused by the FGFR3 A391E mutation, severe achondroplasia with developmental delay caused by the FGFR3 K650M mutation, and thanatophoric dysplasia caused by the FGFR3 R248C mutation (57–61). Acne is a skin feature of Apert syndrome caused by the FGFR2 S252W or P253R mutation (23, 62). The mechanism by which only certain mutations of the FGFRs lead to cutaneous features is not well understood, but it is clear that FGFs and their receptors are involved in many early developmental processes (63) and can have effects on many tissue types (35, 64–66). It is possible that certain FGFR mutations differentially activate certain downstream signaling pathways, whose effects are targeted at specific tissues or organs. It is also possible that there is a threshold effect and that skin abnormalities will occur if there is activation of the FGFR signaling caused by different mechanisms reaching the threshold.

In our BSS mouse model, the phenotype of BSS is consistent with the effect of the Y394C mutation on both FGFR isoforms. FGFR2 IIIb is mainly expressed in epithelial-derived skin tissue; FGFR2 IIIc is primarily expressed in mesenchymal-derived calvarial tissue (37, 41–43). The Y394C mutation involves the gain of a cysteine in the juxtamembrane domain of FGFR2. It has been shown by molecular modeling that the unpaired cysteines promote intermolecular disulfide bond formation, leading to dimerization of the mutant receptors and ligand-independent or constitutive FGFR activation (67, 68). Our results, which demonstrate that FGFR2 is constitutively activated in RCS chondrocytes transfected with the human FGFR2 Y375C mutation as well as in epidermal keratinocytes of $Fgfr2^{+/Y394C}$ mice, are consistent with this model. Interestingly, constitutive activation of other FGFR2 or FGFR3 mutations located in different protein domains causes both skeletal and skin phenotypes, including FGFR3 A391E mutation in the transmembrane domain, K650M mutation in the tyrosine kinase domain, and R248C mutation in the extracellular domain (61, 69), suggesting that the mechanisms of constitutive activation converge to downstream signaling molecules, causing similar skin or skull phenotypes in these conditions.

We have provided evidence that constitutively activated FGFR2 controls abnormal skin and skull development by regulating p38 MAPK. We found that phosphorylated p38 signaling is increased in both the epidermis and calvarial tissues of $Fgfr2^{+/Y394C}$ mice. It is known that p38 is one of the critical components within the downstream signaling pathways of different tyrosine kinase receptors, which are associated with skin development and disorders, including FGFR, EGFR, and IGF1 receptor (IGF1R) (70). Also, p38 signaling is involved in skin homeostasis or epidermal differentiation (71) and plays an important role in osteoblast differentiation (72, 73). Activation of the p38 pathway has been associated with craniosynostosis in Apert syndrome mice with the FGFR2 P253R mutation (49). Other intracellular signaling pathways important to skin hyperplasia or craniosynostosis include ERK and PKCα pathways in craniosynostosis of Apert syndrome $Fgfr2^{+/S252W}$ mice and osteoblasts of patients with Apert syndrome (33, 47, 49–51) as well as

ERK and AKT pathways in keratinocytes of human benign or malignant AN (74–76). Therefore, although we provide strong evidence for the role of the p38 pathway in skin and skeleton development, other parallel or downstream pathways may modulate the effects.

p38 Signaling is the first intracellular pathway involved in skin abnormalities related to craniosynostosis that has been demonstrated in an in vivo animal model. We further confirmed our findings by showing obvious suppression of the skin anomalies by selective inhibition of p38 signaling systemically. Our initial assessments suggest that the p38 inhibition ameliorates the skull abnormalities in BSS to a lesser degree. Because p38 plays a crucial role in the signaling cascades of diverse cellular processes, systemic p38 inhibition could result in undesired pharmacological activities in different organs, as suggested by previous studies (70). Thus, we performed topical administration on the skin and found obvious improvement of skin abnormalities. The effect of p38 inhibition on skin abnormalities in our mice suggests that FGFR2-mediated p38 activation is an important molecular pathogenesis of the skin phenotype in BSS and that the p38 pathway could be a potential pharmacologic target for the treatment of the skin abnormalities.

Interestingly, we saw activation of another important MAPK pathway, ERK1/2, in the skull of $Fgfr2^{+/Y394C}$ mice, whereas the activation of this pathway was not striking in the skin of $Fgfr2^{+/Y394C}$ mice. Further, the ERK1/2 pathway was not inhibited at the drug dosage used and did not contribute to rescuing skin and skull phenotypes. Similarly, the treatment of Apert syndrome $Fgfr2^{+/S252W}$ mice with a p38 inhibitor did not show obvious improvement of the craniosynostosis. These results may reflect the different functional effects of the FGFR2 Y394C and FGFR2 S252W mutations on the receptors and downstream signaling pathways in different tissues. In our BSS mouse model, we speculate that FGFR2 Y394C mutation causes differential activation of the downstream intracellular pathways of FGFR2 in the skin and skull, with greater p38 and less ERK1/2 activation in keratinocytes and greater ERK1/2 and less p38 activation in osteoblasts.

We now know that these different FGFR2 mutations result in different mechanisms. The FGFR2 receptor with the Y394C mutation is constitutively activated, triggering abnormal p38 signaling pathways without the presence of ligand, whereas in Apert syndrome, the receptors with S252W and P253R mutations and ERK1/2 pathways are activated in a ligand-dependent manner (77, 78). Also, p38 signaling appears to have a stronger effect on skin hyperplasia than ERK1/2 signaling, which is important in the etiology of FGFR-related craniosynostosis. Thus, inhibition with p38 or other components of the FGFR network may need to be tailored to optimize the therapeutic effects on diverse organs such as the treatment of skin and skull anomalies in BSS and potentially other common conditions of skin hyperplasia or craniosynostosis.

Methods

Generation of targeting construct and mutant allele genotyping. See Supplemental Methods.

Skeletal staining and histological analysis. Skeletal staining with Alizarin red S and Alcian blue was performed according to published methods (79). Histological sections (5 μm) were prepared from selected tissues that had been fixed in 4% paraformaldehyde for 24–48 hours and embedded in paraffin. Sections were stained with H&E for histology. We studied the coronal sutures by sectioning the head with a sagittal plane using the anterior-posterior axis from the nose to vertebra. The sections analyzed were selected from the middle third portion of the unilateral coronal suture.

Epidermal and dermal thickness measurements and melanin staining. Epidermal thickness was assessed using 2 methods. Initially, ImageJ (http://rsb.info.nih.gov/ij/index.html) analysis of H&E-stained sections was used to quantify epidermal thickness. In each image, 5 different areas were analyzed, and these measurements were repeated on 2 to 4 different pictures for each mouse. Results were obtained from control mice at P0 ($n = 3$), treated mice at P0 ($n = 2$), and both control and treated mice at P5 ($n = 2$ each). Epidermal thickness measurement was further validated using an ocular micrometer in a Nikon Labophot 2 microscope by 2 observers (X. Zhou and R. Phelps). From 6 to 12 measurements were taken from the top of the stratum granulosum to the stratum basale. Dermal thickness measurements were taken at the same time at P0 and P5 from the base of the stratum basale to the top of the panniculus carnosus. Melanin was stained using the Masson-Fontana method. The areas chosen for study of the epidermis and melanin were from the upper dorsal back in all slides.

High-resolution micro-CT image acquisition and landmark data analysis. P0 and P8 mice were sacrificed and fixed in 4% paraformaldehyde. High-resolution microcomputed tomography (HRCT) images of all skulls were acquired at the Center for Quantitative X-Ray Imaging at Pennsylvania State University using an OMNI-X Universal HD600 Industrial X-ray CT system (Bio-Imaging Research Inc). Images of 21 P0 mice ($n = 12$ +/Y394C; 9 +/+) and 24 P8 mice (10 +/Y394C; 14 +/+) were acquired at 16- to 21-μm slice thickness and 15- to 20-μm pixel resolution. A standard minimum threshold of 92 mg/cm³ partial density of hydroxyapatite was used to create bone surfaces for morphometric analysis. The 3D coordinates of 40 biologically relevant cranial landmarks at P0 and 39 landmarks at P8 were recorded for all of the mice using AVIZO (Visualization Sciences Group). Previous analyses have demonstrated the accuracy and precision of this data collection method for CT scans (80, 81).

Differences in craniofacial shape between $Fgfr2^{+/Y394C}$ and nonmutant littermates were assessed separately for P8 and P0 mice using Euclidian Distance Matrix Analysis (EDMA) (82). Linear distances between all unique pairs of landmarks were calculated and were scaled to the geometric mean of all linear distances to account for differences in scale; the ratios between average linear distances for mutants and unaffected littermates were produced. The null hypothesis of similarity in form between mutant and nonmutant crania was evaluated for each linear distance by bootstrap-based 90% CIs, enabling localization of differences to specific anatomic loci.

Immunohistochemical, TUNEL, and ALP assays. Immunohistochemical assays were performed using the VECTOR M.O.M. Immunodetection Kit (Vector Laboratories) for BrdU (Sigma-Aldrich), Ki67 (Vector Laboratories), K14, K10, and loricrin (Novocastra). For BrdU labeling, pregnant female mice were injected with a 10 mg/ml solution of BrdU (Sigma-Aldrich) at 100 μg/g body weight 2 hours before sacrifice. The sections were counterstained with hematoxylin. Cell proliferation of the skin was analyzed by counting the number of Ki67-positive cells in a defined area at the back of the neck where AN occurs more severely in both humans (3) and, according to our observations, in mice. Cell proliferation of the skull was analyzed by calculating the ratios of the number of BrdU-positive cells to total cells between and including the osteogenic fronts. The counts for Ki67- and BrdU-positive cells in mutant and WT embryos were compared by using the t test. The TUNEL assay was done using the In Situ Cell Death Detection Kit, POD (Roche Applied Science) to detect apoptotic cell death by light microscopy. ALP staining was carried out as described (48). For each staining, at least 2 litters of mice were examined.

In situ hybridization. In situ hybridization was performed on sections as described by Wilkinson (83) with modifications. Mouse osteonectin cDNA fragments were each cloned into the pCRII-TOPO Vector (Invitrogen). The plasmids were linearized and antisense and sense single-stranded RNA probes were generated using T7, T3, or SP6 RNA polymerase with digoxigenin (Roche). At least 2 litters of mice were examined.

In vitro FGFR2 functional study. RCS chondrocytes were transfected using FuGENE 6 reagent according to the manufacturer's protocol (Roche Applied Science). Vector-expressing WT FGFR2 was generated by cloning full-length human FGFR2 ORF into the pcDNA3.1 vector, according to the manufacturer's protocol (Invitrogen). Y375C FGFR2 mutant was created by site-directed mutagenesis, according to manufacturer's protocol (QuikChange II Site-Directed Mutagenesis Kit; Agilent Technologies). Empty plasmid was pcDNA3.1. At 36 hours after transfection, cells were lysed in ice-cold lysis buffer supplemented with proteinase inhibitors. Protein samples were resolved by SDS-PAGE, transferred onto a PVDF membrane (Bio-Rad), and visualized by luminescence (Amersham). The following antibodies were used: P-FGFR (Y653/Y654), P-FRS2 (Y196/Y436) (Cell Signaling Technology); FGFR2, ACTIN, and FRS2 (Santa Cruz Biotechnology Inc.). Keratinocyte culture and in vivo FGFR2 functional studies are included in the Supplemental Methods.

Protein preparation and Western blotting. Keratinocyte, epidermis, and calvarial tissues of skull vault were separately isolated by microdissection from P0 pups or E17.5 embryos from at least 2 different litters each of mutant *Fgfr2[+/Y394C]* mice and WT controls. These tissue samples were homogenized in T-PER Tissue Protein Extraction Reagent (Thermo Scientific) using a pellet pestle motor homogenizer (Kontes). Protein concentration was determined with Pre-Diluted Protein Assay Reagent (Pierce). Freshly isolated protein was loaded in equal amounts and resolved on a 4%–15% SDS-PAGE gel. Proteins were electrotransferred to PVDF membrane (Bio-Rad), incubated with the specific antibodies, and visualized by ECL Plus Western Blotting Detection System (Amersham). To ensure consistency in technique, Western blot analysis was performed independently at least twice for each protein sample. The antibodies used were against Fgfr2 (Santa Cruz); PY-100 (Cell Signaling); phospho-p38 (Cell Signaling), total p38 (Cell Signaling); phospho-ERK1/2 (Cell Signaling), total ERK (Cell Signaling); phospho-AKT (Cell Signaling), total AKT (Cell Signaling); phospho-SAPK/JNK (Cell Signaling), total SAPK/JNK (Cell Signaling); and β-actin (Sigma-Aldrich). The levels of protein expression were quantified using the ChemiImager (Cell Biosciences) and normalized relative to the expression of the control, β-actin. The comparison of protein levels was done by calculating the ratio of the normalized phosphorylated protein level to total protein level of the mutant to WT. To compare the median phosphorylation ratio of mutant samples to WT (ratio = 1), 1-sample Wilcoxon's test was used. Statistical significance was assigned at $P < 0.05$. All statistical analyses were performed using SAS/STAT software (SAS Institute Inc.). The scatter plots were generated by GraphPad Prism 5. At least 2 litters of mice were examined.

In utero and topical pharmacological treatment of animals with p38 inhibitor. For treatment of animals, 1.0 mg of SB203580 (Calbiochem) was dissolved in 200 μl 1× PBS, and a dose of 25 mg of the drug/kg body weight/d was used. 1.0 mg of ERK inhibitor U0126 (Cell Signaling) was dissolved in 5% DMSO in 1× PBS, and a dose of 5 mg of the drug/kg body weight/d was used. The drugs were injected intraperitoneally into pregnant mice with BSS FGFR2 Y394C/+ mutation or Apert FGFR2 S252W/+ mutation from E12 through E18 because these are the critical stages for mouse skin and skull development. The intraperitoneal injection of both drugs has been investigated previously in preclinical mouse models for treatment of different induced diseases without skin or skull abnormalities (47, 84). Injection of the vehicle alone (1× PBS or 5% DMSO) was used as a control. Topical treatment of the back skin of the mouse was performed with 100 μM SB203580 dissolved in acetone or acetone-vehicle controls, which was applied to the neck and back skin of the pups from P2 to P5, twice daily. Acetone has been extensively used as a drug vehicle for skin topical application in mice (85). The treated skin or skull was inspected by histological examination from serial views of each *Fgfr2[+/Y394C]* mouse as well as the littermate controls. For both in utero and topical treatment, at least 3 litters of mice were treated and examined.

Statistics. Results are presented as mean ± SEM, with *n* equal to the number of samples analyzed. Significance was determined by unpaired Student's *t* test, and $P \leq 0.05$ was considered statistically significant. For quantification analysis of Ki67, BrdU, TUNEL staining, and skin thickness measurement, we analyzed mice from 2 or 3 litters, which showed consistent results. 3D landmark data collected from high resolution microcomputed tomographic images were analyzed by Euclidean distance matrix analysis (EDMA) (82), and significant differences were determined by bootstrap confidence intervals ($\alpha \leq 0.10$).

Study approval. All animal studies were reviewed and approved by the Johns Hopkins University and Mount Sinai School of Medicine Animal Care and Use Committees and were conducted according to those committees' guidelines.

Address correspondence to: Ethylin Wang Jabs, Department of Genetics and Genomic Sciences, Mount Sinai School of Medicine, One Gustave L. Levy Place, Box 1497, 1428 Madison Avenue, New York, New York, 10029, USA. Phone: 212.241.3504; Fax: 212.241.7112; E-mail: ethylin.jabs@mssm.edu.

1. Beare JM, Dodge JA, Nevin NC. Cutis gyratum, acanthosis nigricans and other congenital anomalies. A new syndrome. *Br J Dermatol.* 1969; 81(4):241–247.
2. Stevenson RE, Ferlauto JG, Taylor HA. Cutis gyratum and acanthosis nigricans associated with other anomalies: A distinctive syndrome. *J Pediatr.* 1978;92(6):950–952.
3. Hall BD, Cadle RG, Golabi M, Morris CA, Cohen MM Jr. Beare-Stevenson cutis gyrata syndrome. *Am J Med Genet.* 1992;44(1):82–89.
4. Vargas RA, et al. Beare-Stevenson syndrome: Two South American patients with FGFR2 analysis. *Am J Med Genet A.* 2003;121A(1):41–46.
5. Stuart CA, Pate CJ, Peters EJ. Prevalence of acanthosis nigricans in an unselected population. *Am J Med.* 1989;87(3):269–272.
6. Rogers DL. Acanthosis nigricans. *Semin Dermatol.* 1991;10(3):160–163.
7. Schwartz RA. Acanthosis nigricans. *J Am Acad Dermatol.* 1994;31(1):1–19.
8. Brown J, Winkelmann RK. Acanthosis nigricans: A study of 90 cases. *Medicine.* 1968;47(1):33–51.
9. Dunaif A, Green G, Phelps RG, Lewohl M, Futterwiet W, Lewy L. Acanthosis nigricans, insulin action and hyperandrogenism: Clinical, histological and biochemical findings. *J Clin Endocrin Metab.* 1991;73(3):590–595.
10. Cohen MM, Maclean RE, eds. *Craniosynostosis: Diagnosis, Evaluation, And Management.* New York, New York, USA; Oxford University Press; 2000.
11. Cohen MM Jr. The new bone biology: Pathologic, molecular, and clinical correlates. *Am J Med Genet A.* 2006;140(23):2646–2706.
12. Becker DB, Petersen JD, Kane AA, Cradock MM, Pilgram TK, Marsh JL. Speech, cognitive, and behavioral outcomes in nonsyndromic craniosynostosis. *Plast Reconstr Surg.* 2005;116(2):400–407.
13. Boulet SL, Rasmussen SA, Honein MA. A pop-

ulation-based study of craniosynostosis in metropolitan Atlanta, 1989–2003. *Am J Med Genet A*. 2008;146A(8):984–991.

14. Przylepa KA, et al. Fibroblast growth factor receptor 2 mutations in Beare-Stevenson cutis gyrata syndrome. *Nat Genet*. 1996;13(4):492–494.

15. Hsu TY, Chang SY, Wang TJ, Ou CY, Chen ZH, Hsu PH. Prenatal sonographic appearance of Beare Stevenson cutis gyrata syndrome: Two- and three-dimensional ultrasonographic findings. *Prenat Diagn*. 2001;21(8):665–667.

16. Akai T, Iizuka H, Kishibe M, Kawakami S, Kobayashi A, Ozawa T. A case of Beare-Stevenson cutis gyrata syndrome confirmed by mutation analysis of the fibroblast growth factor receptor 2 gene. *Pediatr Neurosurg*. 2002;37(2):97–99.

17. Wang TJ, Huang CB, Tsai FJ, Wu JY, Lai RB, Hsiao M. Mutation in the FGFR2 gene in a Taiwanese patient with Beare-Stevenson cutis gyrata syndrome. *Clin Genet*. 2002;61(3):218–221.

18. Eun SH, et al. The first Korean case of Beare-Stevenson syndrome with a Tyr375Cys mutation in the fibroblast growth factor receptor 2 gene. *J Korean Med Sci*. 2007;22(2):352–356.

19. Fonseca R, Costa-Lima MA, Cosentino V, Orioli IM. Second case of Beare-Stevenson syndrome with an FGFR2 Ser372Cys mutation. *Am J Med Genet A*. 2008;146A(5):658–660.

20. Ornitz DM, Marie PJ. FGF signaling pathways in endochondral and intramembranous bone development and human genetic disease. *Genes Dev*. 2002;16(12):1446–1465.

21. Fuchs E. Skin stem cells: rising to the surface. *J Cell Biol*. 2008;180(2):273–284.

22. Hajihosseini MK. Fibroblast growth factor signaling in cranial suture development and pathogenesis. *Front Oral Biol*. 2008;12:160–177.

23. Katoh M. FGFR2 abnormalities underlie a spectrum of bone, skin, and cancer pathologies. *J Invest Dermatol*. 2009;129(8):1861–1867.

24. Fuchs E, Raghavan S. Getting under the skin of epidermal morphogenesis. *Nat Rev Genet*. 2002; 3(3):199–209.

25. Opperman LA. Cranial sutures as intramembranous bone growth sites. *Dev Dyn*. 2000; 219(4):472–485.

26. Werner S, et al. The function of KGF in morphogenesis of epithelium and reepithelialization of wounds. *Science*. 1994;266(5186):819–822.

27. LaRochelle WJ, et al. Specific receptor detection by a functional keratinocyte growth factor-immunoglobulin chimera. *J Cell Biol*. 1995;129(2):357–366.

28. Petiot A, Conti FJ, Grose R, Revest JM, Hodivala-Dilke KM, Dickson C. A crucial role for Fgfr2-IIIb signalling in epidermal development and hair follicle patterning. *Development*. 2003;130(22):5493–5501.

29. Steiling H, Werner S. Fibroblast growth factors: key players in epithelial morphogenesis, repair and cytoprotection. *Curr Opin Biotechnol*. 2003; 14(5):533–537.

30. Grose R, et al. The role of fibroblast growth factor receptor 2b in skin homeostasis and cancer development. *EMBO J*. 2007;26(5):1268–1278.

31. Yang J, et al. Fibroblast growth factor receptors 1 and 2 in keratinocytes control the epidermal barrier and cutaneous homeostasis. *J Cell Biol*. 2010; 188(6):935–952.

32. Eswarakumar VP, Lax I, Schlessinger J. Cellular signaling by fibroblast growth factor receptors. *Cytokine Growth Factor Rev*. 2005;16(2):139–149.

33. Marie PJ, Kaabeche K, Guenou H. Roles of FGFR2 and twist in human craniosynostosis: Insights from genetic mutations in cranial osteoblasts. *Front Oral Biol*. 2008;12:144–159.

34. Melville H, Wang Y, Taub PJ, Jabs EW. Genetic basis of potential therapeutic strategies for craniosynostosis. *Am J Med Genet A*. 2010;152A(12):3007–3015.

35. Miraoui H, Marie PJ. Fibroblast growth factor receptor signaling crosstalk in skeletogenesis. *Sci Signal*. 2010;3(146):re9.

36. Mailleux AA, et al. Role of FGF10/FGFR2b signaling during mammary gland development in the mouse embryo. *Development*. 2002;129(1):53–60.

37. Eswarakumar VP, Monsonego-Ornan E, Pines M, Antonopoulou I, Morriss-Kay GM, Lonai P. The IIIc alternative of Fgfr2 is a positive regulator of bone formation. *Development*. 2002;129(16):3783–3793.

38. Johnson DE, Lee PL, Lu J, Williams LT. Diverse forms of a receptor for acidic and basic fibroblast growth factors. *Mol Cell Biol*. 1990;10(9):4728–4736.

39. Ornitz DM, Itoh N. Fibroblast growth factors. *Genome Biol*. 2001;2(3): REVIEWS3005.

40. Schlessinger J, Mohammadi M. Insights into the molecular basis for fibroblast growth factor receptor autoinhibition and ligand-binding promiscuity. *Proc Natl Acad Sci U S A*. 2004;101(4):935–940.

41. Miki T, et al. Determination of ligand-binding specificity by alternative splicing: two distinct growth factor receptors encoded by a single gene. *Proc Natl Acad Sci U S A*. 1992;89(1):246–250.

42. Orr-Urtreger A, et al. Developmental localization of the splicing alternatives of fibroblast growth factor receptor-2 (FGFR2). *Dev Biol*. 1993;158(2):475–486.

43. Ornitz DM, et al. Receptor specificity of the fibroblast growth factor family. *J Biol Chem*. 1996; 271(25):15292–15297.

44. Schlessinger J. Cell signaling by receptor tyrosine kinases. *Cell*. 2000;103(2):211–225.

45. Dailey L, Ambrosetti D, Mansukhani A, Basilico C. Mechanisms underlying differential responses to FGF signaling. *Cytokine Growth Factor Rev*. 2005; 16(2):233–247.

46. Khavari TA, Rinn J. Ras/Erk MAPK signaling in epidermal homeostasis and neoplasia. *Cell Cycle*. 2007; 6(23):2928–2931.

47. Shukla V, Coumoul X, Wang RH, Kim HS, Deng CX. RNA interference and inhibition of MEK-ERK signaling prevent abnormal skeletal phenotypes in a mouse model of craniosynostosis. *Nat Genet*. 2007;39(9):1145–1150.

48. Wang Y, et al. Abnormalities in cartilage and bone development in the Apert syndrome FGFR2(+/S252W) mouse. *Development*. 2005; 132(15):3537–3548.

49. Wang Y, et al. Activation of p38 MAPK pathway in the skull abnormalities of Apert syndrome Fgfr2(+/P253R) mice. *BMC Dev Biol*. 2010;10:22.

50. Yin L, et al. A Pro253Arg mutation in fibroblast growth factor receptor 2 (Fgfr2) causes skeleton malformation mimicking human Apert syndrome by affecting both chondrogenesis and osteogenesis. *Bone*. 2008;42(4):631–643.

51. Holmes G, Rothschild G, Roy UB, Deng CX, Mansukhani A, Basilico C. Early onset of craniosynostosis in an Apert mouse model reveals critical features of this pathology. *Dev Biol*. 2009;328(2):273–284.

52. Ong SH, Hadari YR, Gotoh N, Guy GR, Schlessinger J, Lax I. Stimulation of phosphatidylinositol 3-kinase by fibroblast growth factor receptors is mediated by coordinated recruitment of multiple docking proteins. *Proc Natl Acad Sci U S A*. 2001; 98(11):6074–6079.

53. Yong HY, Koh MS, Moon A. The p38 MAPK inhibitors for the treatment of inflammatory diseases and cancer. *Expert Opin Investig Drugs*. 2009; 18(12):1893–1905.

54. Mayer RJ, Callahan JF. p38 MAP kinase inhibitors: a future therapy for inflammatory diseases. *Drug Discov Today*. 2006;3:49–54.

55. Logié A, et al. Activating mutations of the tyrosine kinase receptor FGFR3 are associated with benign skin tumors in mice and humans. *Hum Mol Genet*. 2005;14(9):1153–1160.

56. Wolfram JA, et al. Keratinocyte but not endothelial cell-specific overexpression of Tie2 leads to the development of psoriasis. *Am J Pathol*. 2009;

174(4):1443–1458.

57. Meyers GA, Orlow SJ, Munro IR, Przylepa KA, Jabs EW. Fibroblast growth factor receptor 3 (FGFR3) transmembrane mutation in Crouzon syndrome with acanthosis nigricans. *Nat Genet*. 1995;11(4):462–464.

58. Wilkes D, et al. A recurrent mutation, ala391glu, in the transmembrane region of FGFR3 causes Crouzon syndrome and acanthosis nigricans. *J Med Genet*. 1996;33(9):744–748.

59. Bellus GA, et al. Severe achondroplasia with developmental delay and acanthosis nigricans (SADDAN): Phenotypic analysis of a new skeletal dysplasia caused by a Lys650Met mutation in fibroblast growth factor receptor 3. *Am J Med Genet*. 1999;85(1):53–65.

60. Passos-Bueno MR, Wilcox WR, Jabs EW, Sertié AL, Alonso LG, Kitoh H. Clinical spectrum of fibroblast growth factor receptor mutations. *Hum Mutat*. 1999;14(2):115–125.

61. Tavormina PL, et al. A novel skeletal dysplasia with developmental delay and acanthosis nigricans is caused by a Lys650Met mutation in the fibroblast growth factor receptor 3 gene. *Am J Hum Genet*. 1999;64(3):722–731.

62. Melnik BC. Role of FGFR2-signaling in the pathogenesis of acne. *Dermatoendocrinol*. 2009;1(3):141–156.

63. Dorey K, Amaya E. FGF signalling: diverse roles during early vertebrate embryogenesis. *Development*. 2010;137(22):3731–3742.

64. Ford-Perriss M, Abud H, Murphy M. Fibroblast growth factors in the developing central nervous system. *Clin Exp Pharmacol Physiol*. 2001;28(7):493–503.

65. Suhardja A, Hoffman H. Role of growth factors and their receptors in proliferation of microvascular endothelial cells. *Microsc Res Tech*. 2003;60(1):70–75.

66. Degnin CR, Laederich MB, Horton WA. FGFs in endochondral skeletal development. *J Cell Biochem*. 2010;110(5):1046–1057.

67. Neilson KM, Friesel RE. Constitutive activation of fibroblast growth factor receptor-2 by a point mutation associated with Crouzon syndrome. *J Biol Chem*. 1995;270(44):26037–26040.

68. Wilkie AO, et al. Apert syndrome results from localized mutations of FGFR2 and is allelic with Crouzon syndrome. *Nat Genet*. 1995;9(2):165–172.

69. Chen F, Degnin C, Laederich M, Horton WA, Hristova K. The A391E mutation enhances FGFR3 activation in the absence of ligand. *Biochim Biophys Acta*. 2011;1808(8):2045–2050.

70. Chopra P, Kanoje V, Semwal A, Ray A. Therapeutic potential of inhaled p38 mitogen-activated protein kinase inhibitors for inflammatory pulmonary diseases. *Expert Opin Investig Drugs*. 2008; 17(10):1411–1425.

71. Efimova T. p38delta mitogen-activated protein kinase regulates skin homeostasis and tumorigenesis. *Cell Cycle*. 2010;9(3):498–505.

72. Hu Y, Chan E, Wang SX, Li B. Activation of p38 mitogen-activated protein kinase is required for osteoblast differentiation. *Endocrinology*. 2003; 144(5):2068–2074.

73. Wang X, Goh CH, Li B. p38 mitogen-activated protein kinase regulates osteoblast differentiation through osterix. *Endocrinology*. 2007;148(4):1629–1637.

74. Haase I, Hunzelmann N. Activation of epidermal growth factor receptor/ERK signaling correlates with suppressed differentiation in malignant acanthosis nigricans. *J Invest Dermatol*. 2002;118(5):891–893.

75. Torley D, Bellus GA, Munro CS. Genes growth factors and acanthosis nigricans. *Br J Dermatol*. 2002; 147(6):1096–1101.

76. Higgins SP, Freemark M, Prose NS. Acanthosis nigricans: A practical approach to evaluation and management. *Dermatol Online J*. 2008;14(9):2.

77. Anderson J, Burns HD, Enriquez-Harris P, Wilkie AO, Heath JK. Apert syndrome mutations in fibroblast growth factor receptor 2 exhibit increased

affinity for FGF ligand. *Hum Mol Genet*. 1998; 7(9):1475–1483.

78. Yu K, et al. Conditional inactivation of FGF receptor 2 reveals an essential role for FGF signaling in the regulation of osteoblast function and bone growth. *Development*. 2003;130(13):3063–3074.

79. Hogan B, Beddington R, Constantini F, Lacy E, eds. Staining embryos for cartilage and bone. In: *Manipulating the Mouse Embryo: A Laboratory Manual*. Cold Spring Harbor, New York, USA: Cold Spring Harbor Laboratory Press; 1994:379.

80. Richtsmeier JT, Paik CH, Elfert PC, Cole TM 3rd, Dahlman HR. Precision, repeatability, and validation of the localization of cranial landmarks using computed tomography scans. *Cleft Palate Craniofac J*. 1995;32(3):217–227.

81. Corner BD, Lele S, Richtsmeier JT. Measuring precision of three-dimensional landmark data. *J Quant Anthropol*. 1992;3(4):347–359.

82. Lele S, Richtsmeier JT, eds. An invariant approach to statistical analysis of shapes. In: *Interdisciplinary Studies In Statistics Series*. London, United Kingdom; Chapman and Hall–CRC Press; 2001.

83. Wilkinson DG, eds. *In Situ Hybridization: A Practical Approach*. London, United Kingdom: Oxford University Press; 1992.

84. Costantini TW, et al. Role of p38 MAPK in burn-induced intestinal barrier breakdown. *J Surg Res*. 2009;156(1):64–69.

85. Bracht L, Caparroz-Assef SM, Magon TF, Ritter AM, Cuman RK, Bersani-Amado CA. Topical anti-inflammatory effect of hypocholesterolaemic drugs. *J Pharm Pharmacol*. 2011;63(7):971–975.